The thermal equation of state of the magma Ocean

Razvan Caracas

Earth Planet. Sci. Lett. 637 (2024) 118724

Contents lists available at ScienceDirect

Earth and Planetary Science Letters

journal homepage: www.elsevier.com/locate/epsl

The thermal equation of state of the magma Ocean

Razvan Caracas [a, b, *]

[a] Institut de Physique du Globe de Paris, Université Paris Cité, CNRS, 1 rue Jussieu Paris 75005 France
[b] Center for Planetary Habitability, University of Oslo, Blindern, Oslo, Norway

ARTICLE INFO

Keywords:
Magma ocean
Equation of state
Thermal dilatation
Compressibility
Evolution
Early earth, Molecular dynamics
Ab initio
Melts
Liquid structure
Viscosity

ABSTRACT

As the protolunar disk formed by the giant impact with the incoming asteroid Theia started to cool, the Earth condensed in its center as a molten planet. The outer layer, rich in lithophile oxides, formed the magma ocean, whose dynamical behavior heavily influenced the entire evolution of the early Earth. Here, we employ first-principles molecular dynamics simulations to characterize the magma ocean in its initial stage. We compute the compressibility and the viscosity of the molten pyrolite, which best approximates the bulk silicate Earth composition. With an extensive set of calculations, we span the entire relevant pressure-temperature range. We provide a detailed analysis of the athermal and thermal equations of state in various formulations. We obtain a linear temperature dependence for the bulk modulus using the 4th order Birch-Murnaghan equation of state. We show that the liquid silicate accommodates compression by the collapse of the second Si-O coordination sphere, whose corresponding coordination number passes from about 24 at the surface of the magma ocean to about 40 at its deepest point. We found that pyrolite melts have a very low viscosity, about one order of magnitude lower than that of molten basalt. We also propose a revised position of the critical point of the bulk silicate Earth, which lies around 6000 K and 1.1–1.2 kbars.

1. Introduction

It is widely accepted that most terrestrial planets and planetesimal went through stages of partial or global magma oceans during their accretion time (Elkins-Tanton, 2012; Greenwood et al., 2005; Kite et al., 2021; Schaefer and Elkins-Tanton, 2018; Sturtz et al., 2022a, 2022b). The energy, first originating from radioactive decay and later from successive impacts, was sufficient to at least partially melt the outer layer of oxides and silicates – the mantle (Dodds et al., 2021; Kaminski et al., 2020; Neumann et al., 2012). As a result of this melting, all the planetesimals larger than several tens of kms in diameter are expected to have differentiated into at least two layers: the oxide-based mantle and the iron-based core.

The lifetime of the molten state at the surface depended on a series of factors, like loss of energy to space, presence of volatiles dissolved in the melt, presence of a thermally protecting atmosphere, amount of radioactivity, etc. Modeling the evolution of the magma ocean helps us understand the crystallization process in depth (Ballmer et al., 2017) as well as the formation of the crust at the surface. There are several key parameters that we need to know and to understand in order to perform such a modeling. Amongst them, the equation of state of the liquid, which represents the densification of the molten silicate with pressure and temperature, and the viscosity of the liquid, are some of the fundamental functions required by the modeling.

Despite its importance, measuring experimentally the density of a melt is a daunting task (Aksay et al., 1979; Sanloup, 2016; Sanloup et al., 2013). For crystals, X-ray diffraction measurements of the unit cell parameters are straightforward today and provide relatively easy, accurate equations of state. But melts do not have such a periodically repeated unit cell, and consequently, X-ray diffraction is less straightforward in this exercise (Yu et al., 2019). Alternatively, one can measure the volume of the sample at a given pressure and temperature, e.g. from X-ray tomography, and, knowing the initial mass introduced in the experiment and assuming the entire sample is uniformly melted, one could deduce the density of that sample (Liu et al., 2008; Shi et al., 2013). However, samples in diamond-anvil cell experiments are rarely completely molten, because of the high thermal conductivity of diamond (Jephcoat and Besedin, 1996). On the other hand, accurate microtomography can help separate the fraction of melt from a melt-crystal mixture even inside a diamond-anvil cell, and thus, assuming the composition of the molten part is homogenous, obtain the density (Shi et al., 2013). Finally, the densification of glasses under compression (Murakami and Bass,

* Corresponding Author.
E-mail address: caracas@ipgp.fr.

https://doi.org/10.1016/j.epsl.2024.118724
Received 9 November 2023; Received in revised form 13 April 2024; Accepted 16 April 2024
Available online 30 April 2024

2011; Prescher et al., 2017) can offer alternative information about the behavior of a melt under pressure, though these measurements are usually performed at ambient temperatures.

A successful alternative to static experiments is shock studies that reach the melt stability field. They allow the direct measurement of the density of a material at high temperature and pressure. The measurement is done at one specific point along the Hugniot equation, whose position depends on the initial conditions of the sample (density and temperature) and the energy of the shock. Such experiments were previously carried out on a variety of simple and complex silicate melts and glasses (Ahrens, 1995; Asimow, 2012; Baziotis et al., 2022; Miller et al., 2012; Morard et al., 2020; Rigden et al., 1988; Thomas and Asimow, 2013)

Measurements of the viscosity of a molten material come with their own experimental difficulties. They typically consist of measuring the speed of a falling sphere inside a molten silicate with the help of X-ray tomography (Sakamaki and Ohtani, 2022; Stagno et al., 2020; Suzuki et al., 2002).

Here, we take a different approach and compute the density of silicate melts as a function of temperature and pressure. We consider a 6-component silicate melt containing Na_2O, CaO, Al_2O_3, FeO, MgO, and SiO_2, in proportions that reproduce to better than 1 wt% the bulk silicate Earth composition (McDonough and Sun, 1995). We call this melt pyrolite, as in our previous studies (Caracas et al., 2019; Caracas and Stewart, 2023; Solomatova and Caracas, 2019, 2021). Its actual molar composition is $NaCa_2Al_3Fe_4Mg_{30}Si_{24}O_{89}$. We explore the temperature and pressure range characteristics for the global magma ocean. Similar first-principles calculations in the past provided equations of state and/or melting curves of various melts of geological and geodynamical interest, like MgO (Cohen and Gong, 1994; Cohen and Weitz, 1998; Taniuchi and Tsuchiya, 2018), SiO2 (Gonzalez-Cataldo et al., 2016; Mazevet et al., 2015; Usui and Tsuchiya, 2010), MgSiO3 (de Koker et al., 2013; Karki, 2010; Karki et al., 2013; Petitgirard et al., 2015; Stixrude et al., 2009; Stixrude and Karki, 2005), CaSiO3 (Braithwaite and Stixrude, 2019; Hernandez et al., 2022), Mg2SiO4 (de Koker et al., 2008), Fe2SiO4 (Ramo and Stixrude, 2014; Thomas et al., 2012), etc., but, with the notable exception of basalt (Bajgain et al., 2022), they have a rather limited number of components. Here, we study a complex pyrolitic melt that reproduces the bulk silicate Earth and thus best matches the chemical composition of the magma ocean in its early stages of evolution (McDonough and Sun, 1995).

2. Methodology

We perform *ab initio* molecular dynamics (AIMD) simulations in the canonical, NVT, ensemble. N represents the number of particles in the system, V is the specific volume, and T is the temperature. N and V are fixed throughout the simulation, while T is controlled using the Nose-Hoover thermostat (Hünenberger, 2005). T is determined from the kinetic energy of the atoms. The atoms move in the simulations according to interatomic forces. We employ the density-functional theory as implemented in the VASP package in the planar augmented wave-function (Kresse and Hafner, 1993; Kresse and Joubert, 1999) approach to determine the interatomic forces at each time step.

The electronic density is sampled in the reciprocal space in the Gamma point. The simulation boxes contain 306 atoms, *i. e.* two formula units. All the simulations are run in the spin-polarized approach, due to the presence of ferrous iron. We employ the generalized gradient approximation (GGA) for the exchange-correlation term in the Perdew-Burke Erzernhof (PBE) formalism (Perdew et al., 1996). While other functionals might better describe at least some of the physical properties of these melts, here, the use of the PBE version of the GGA makes it easier to compare these results with other studies on both melts and solids, both past and future (Caracas et al., 2023). We take into account the electronic temperature of the system using the standard Fermi-Dirac thermal distribution of the occupancy of the electronic bands.

We use timesteps of 1 femtosecond above 3000 K and 1 or 2 femtoseconds below that. At each simulation, we remove at least the first 500 steps to ensure thermalization, i.e. reaching a normal distribution of the atomic velocities around an average temperature. Most simulations run for at least 4 picoseconds, some going far beyond that. A few points are run at slightly shorter times, as they serve mainly for refining the pressure relations to density. In some cases, we perform several simulations at the same density and temperature but starting with different initial configurations. In all these cases, once thermalization is achieved, the values of the thermodynamic parameters obtained in the individual simulations roughly overlap with each other.

First, we fit one independent athermal equation of state (EOS) for each isotherm. As there is no universal analytical equation of state form for fluids, we decided to employ Birch-Murnaghan equations of state, both at 3rd (BM3) and at 4th (BM4) order (Birch, 1947; Murnaghan, 1944). According to BM4, the pressure (P) is defined to relate to the density (ρ) as:

$$P(\rho) = \frac{3}{2}K_0\left(\left(\frac{\rho}{\rho_0}\right)^{7/3} - \left(\frac{\rho}{\rho_0}\right)^{5/3}\right)\left(1+\frac{3}{4}(K^{'}-4)\left(\left(\frac{\rho}{\rho_0}\right)^{\frac{2}{3}}-1\right)\right. \\ \left. +\frac{3}{8}\left(K_0K^{''}+(K^{'}-3)(K^{'}-4)+\frac{35}{9}\right)\left(\left(\frac{\rho}{\rho_0}\right)^{\frac{2}{3}}-1^2\right)\right) \quad (1)$$

where ρ_0 is the density at $P = 0$ GPa, K_0 represent the compressibility at $P = 0$ GPa, K' and K'' are the first and the second derivatives of the compressibility with respect to pressure.

BM3 is then obtained from BM4 by making $K^{''} = 0$.

To fit a thermal EOS, we adopt the modified Holland-Powell equation (Angel et al., 2014; Holland and Powell, 1998), which relates the volume to temperature via:

$$V_{0T} = V_{00}\left(1+\alpha_0(T-T_0)-2(10\alpha_0-\alpha 1)\left(\sqrt{T}-\sqrt{T_0}\right)\right) \quad (2)$$

Where T is the temperature, T_0 is the reference temperature, V_{0T} and V_{00} are the reference volumes corresponding to the densities ρ and ρ_0), at, respectively, a temperature T and $T = 0$, and α_0 and α_1 are coefficients.

As a further check, we also use the athermal Vinet 3rd order EOS to fit the pressure–density relations along the different individual isotherms:

$$P(\rho) = \frac{3}{2}K_0\left(\frac{\rho}{\rho_0}\right)^{-\frac{2}{3}}\left(1-\left(\frac{\rho}{\rho_0}\right)^{\frac{1}{3}}\right)\exp\left(\frac{3}{2}(K^{'}-1)\left(1-\left(\frac{\rho}{\rho_0}\right)^{\frac{1}{3}}\right)\right) \quad (3)$$

Apart from the pressure determination, we also analyze the Si-O bonding relations at all conditions of our simulations. For this, we employ the UMD package (Caracas et al., 2021), and determine the Si-O pair distribution functions, g(r). They are obtained by calculating the distances between all the Si – O pairs at every time step of every simulation. As is standard procedure, the first maximum of the $g_{Si\text{-}O}(r)$ defines the most likely Si-O bond distance, the distance to the first minimum of the $g_{Si\text{-}O}(r)$ defines the radius of the first coordination sphere, and the integral over the first coordination sphere defines the coordination number (Allen and Tildesley, 1987; Frenkel and Smit, 2002). Similarly, the second peak and the second minimum of the $g_{Si\text{-}O}(r)$ define respectively the most likely Si-O-Cation-O bond distance and the second coordination sphere.

The viscosity of the silicate melt is obtained from the autocorrelation of the shear stresses (Caracas et al., 2021). As this procedure is sensitive to the length of the simulations, we ensured that only the simulations lasting more than 60 ps were treated to obtain the viscosity.

Compared to our previous simulations on molten pyrolite (Caracas et al., 2019; Solomatova and Caracas, 2019, 2021), the current simulations presented here have a better thermal and density resolution (which ensures more reliable EOS), double the number of atoms (which ensures better description of the chemical speciation in the melt), and a

Fermi-Dirac thermal electronic treatment (instead of previously Gaussian treatment, ensuring a better description of the electronic properties at high temperatures). As such, we expect them to be more reliably useful for further geodynamic modeling of the magma ocean.

3. Results and discussion

We run simulations along several isotherms, starting at 2000 K, and increasing the temperature in 500 K steps, up to 6000 K. We consider between 12 and 20 density points at each temperature. We try to avoid exploring too far in the undercooled melt regime, where the system shows no diffusion, rather behaving like a glass. We also exclude from the final analysis the simulations where the pressure is beyond 180 GPa. Thus, we avoid or in the worst case ensure a minimum overlap of the cores of the pseudopotentials, which represents a critical constraint to ensure the validity of the results.

We compute the pressure at each density-temperature point. We take the average of the computed pressure over the entire simulation time to fit the EOS. As is standard procedure in MD simulations, the pressure and temperature fluctuate throughout the simulation. The temperature fluctuation is directly related to the number of atoms in the system and the quality of the thermostat (Allen and Tildesley, 1987). Increasing the number of atoms decreases the amplitude of the fluctuations of both pressure and temperature. While the temperature fluctuations are of no interest in this context, we use the pressure fluctuations as error bars when determining the equations of state. This procedure gives a very conservative estimate of the error bars that is considerably larger than the one obtained from the decorrelation method.

Fig. 1 shows a 3D representation of the pressure variation as a function of density and temperature. Our calculations cover the 2000 – 5500 K temperature range and 1.0 – 6.0 g/cm^3 density range, corresponding to pressures in the 0 – 180 GPa space. Table S1 lists all the relevant values of the thermodynamic parameters, density, temperature, pressure, and pressure fluctuations for each simulation. We also list the total length of each simulation. Most of the simulations last at least 4 ps, with a few exceptions lasting between 2 and 4 ps (see discussion below about the relevance of these results). Some of the points are obtained by averaging results from multiple simulations performed with different initial configurations. As stated above, their individual results are almost identical, which is reassuring. These multiple calculations provide further reliability checks, longer simulations, and better general statistics.

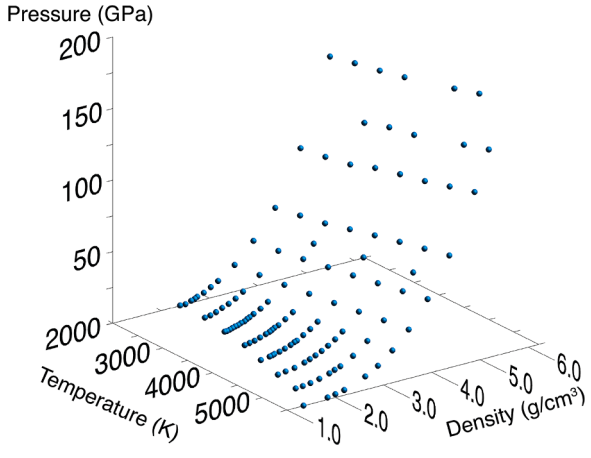

Fig. 1. 3D representation of the pressure variation as a function of density and temperature. Our simulations cover a 1–6 g/cm^3 density range and 2000 – 5500 K temperature range, spanning the entire possible regimes of the magma ocean in the aftermath of its condensation from the protolunar disk.

3.1. Equation of state

The density at ambient pressures is well-defined at low temperatures. At 2000 K, which are our closest temperatures to those of erupting mafic and ultramafic lavas, similar to hotspots, mid-ocean ridge basalts, and ocean island basalts, the computed density of pyrolite is 2.45 g/cm3. The other computed values in the 2000 K – 5500 K temperature range are given in Table 1. The values align themselves along a quasi-linear curve. This validates the Holland-Powell choice for the thermal part of the EOS (see below). The linear fit yields a thermal expansivity of 2.5 × 10^{-4} g/cm^3/K. All the values above 2000 K are directly computed, while below 2000 K they need to be interpolated. The linear interpolation down to 1500 K yields a value of density of 2.53 g/cm^3. A 2nd order polynomial fit on the same data yields a value of 2.52 g/cm^3.

While there are no pyrolite lavas erupting today on the surface of the Earth, we can, nevertheless, compare our results with data of basalts (Lange and Carmichael, 1987; Sanloup, 2016), as examples of contemporary mafic and ultramafic lavas. Measurements of basaltic lavas in Hawaii show densities in the range of 2.3 and 3.0 g/cm3, in shallow environments with little depth-dependence (Moore, 2001). Further measurements on basalt in Iceland put the density between 2.7 to 2.9 g/cm^3, increasing with increasing MgO content (Hartley and Maclennan, 2018).

The theoretical dry pyrolite magmas explored here are slightly lighter than basalts, likely due to smaller amounts of iron oxide and the absence of volatiles in the melt. The temperature of erupting basalts, at about 1500 K, is also slightly smaller than our coolest melts at 2000 K, and the extrapolation of the density is less reliable for such low temperatures.

Table 2 lists the fitted parameters of the BM3 and the BM4 EOS for the molten pyrolite in the 2000 – 6000 K temperature regime. Results from further BM3 fits up to 250 GPa pressure range and the Vinet 3rd order EOS (Eq. (3)) are listed in **Table S2**.

Both the BM3 and the Vinet fits are remarkably good in the 2000 – 5000 K temperature range, and are still usable at 5500 K. Provided enough data points are available, BM4 offers a very good and reliable alternative. For example, at the 3000 K isotherm, BM3 yields χ^2=3.5421 and a goodness of fit of 0.9999, and the BM4 yields χ^2=0.0914 and a goodness of fit of 1. Fig. 2 shows the difference between the actual value of the pressures computed in the MD runs and the BM3 and BM4 fits at 2000 K and 4000 K. The deviations between the actual computed pressure values and those provided by the EOS fits lie within the 1 GPa range. There is always a tradeoff between the different EOS parameters, and the 1 GPa deviation range gives an estimate of the global quality of the EOS fits.

Once we reach about 10 pressure points that are relatively well spread along each isotherm, the fits are close to convergence. However, the length of the simulations needs to reach at least 2 ps, and preferably at least 4 ps, at each simulation point. Otherwise, the pressure values lie

Table 1
The density of pyrolite melts at ambient pressure and different temperatures. The 1500 K value (starred) is obtained by extrapolating a linear temperature dependence of the density below 2000 K.

T (K)	ρ_o (g/cm^3)
1500	2.53*
2000	2.45
2500	2.35
3000	2.27
3500	2.12
4000	1.97
4500	1.83
5000	1.61
5500	1.03

Table 2
The parameters of the athermal 3rd (BM3) and 4th (BM4) order Birch-Murnaghan equations of state (EOS) were obtained by fitting the pressure–density points along isotherms in the 2000 – 5500 K below 180 GPa. Due to the vicinity of the critical temperature, the fits to the 6000 K isotherm data fail. The weighted χ^2 values are less than 0.10; for reference BM4 at 4000 K yields weighted $\chi^2 = 0.03$.

BM3 EOS						
T (K)	K (GPa)	st.dev. K (GPa)	ρ (g/cm^3)	st.dev. ρ (g/cm^3)	Kp	st. dev. Kp
2000	13.06	3.51	2.39	0.07	6.67	0.66
2500	12.80	3.51	2.32	0.08	6.36	0.63
3000	12.38	2.87	2.24	0.06	6.06	0.48
3500	12.01	2.78	2.15	0.07	5.69	0.40
4000	10.76	2.49	2.03	0.07	5.46	0.34
4500	9.02	2.73	1.92	0.09	5.44	0.40
5000	6.52	2.47	1.74	0.11	5.48	0.44
5500	4.24	2.26	1.55	0.14	5.58	0.57

BM4 EOS								
T (K)	K	st.dev. K (GPa)	ρ (g/cm^3)	st.dev. ρ (g/cm^3)	Kp	st. dev. Kp	Kpp	st.dev. Kpp
2000	22.25	5.03	2.46	0.05	4.27	0.80	−0.07	0.11
2500	19.46	4.91	2.38	0.06	4.44	0.90	−0.12	0.17
3000	16.57	2.00	2.28	0.05	4.68	0.65	−0.21	0.17
3500	11.18	4.55	2.14	0.08	6.00	1.50	−0.92	1.15
4000	8.02	4.63	1.99	0.11	6.65	2.10	−1.83	2.87
4500	6.29	5.35	1.86	0.17	6.69	2.77	−2.35	5.04
5000	2.13	7.10	1.58	0.46	9.68	16.55	−20.61	167.30

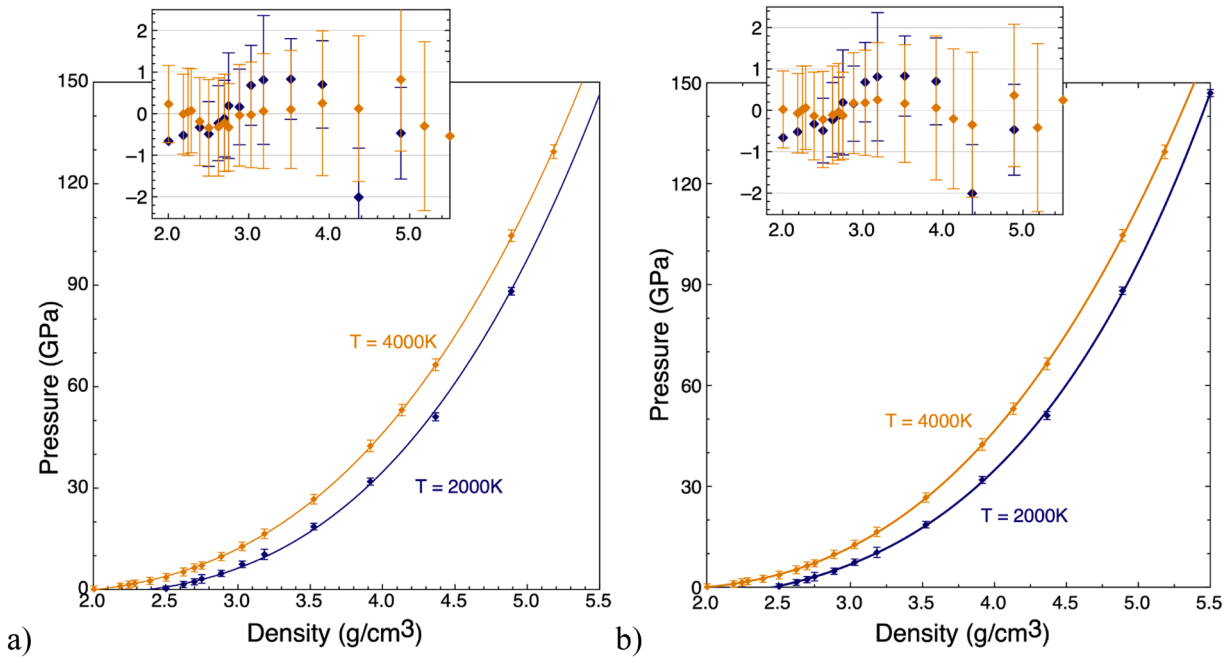

Fig. 2. Comparison between the 3rd order (a) and 4th order (b) Birch-Murnaghan equations of state fits to the computed values of the pressure for molten pyrolite along the 2000 K and 4000 K isotherms. The fits yield pressure values that are very close to the actual calculated points. The error bars on the symbols represent the amplitude of the pressure fluctuations encountered in the simulations.

outside the 1 GPa pressure range above or below the EOS fit. In our setting, with a thermostat mass of 4 VASP units, the pressure and temperature fluctuations have an average period of 20 to 40 fs. The minimum simulation time of 2 ps after thermalization corresponds to at least 50 fluctuations. This value seems to be sufficient for the system to explore enough of the configuration space to correctly describe the macroscopic thermodynamic parameters, like pressure, energy, and temperature. Simulations at given density-temperature conditions starting with different initial configurations yield similar pressure and energy values, with overlapping fluctuations ranges.

The athermal BM4 EOS fits on molten pyrolite yield a density at 20 GPa of 3.58 g/cm^3 at 2000 K, 3.53 at 2500 K, and 3.47 at 3000 K. For comparison, depending on the experimental run and the composition, peridotitic melts at 20 GPa have estimated densities of about 3.6 g/cm^3 at 2633 K (Suzuki et al., 1998) and about 3.55 at 2300 K (Suzuki and Ohtani, 2003). However, extrapolations from low-pressure experiments put the density of peridotite melt to about 3.75 g/cm^3 at 2300 K.

But the most interesting aspects of the magma ocean reside in its thermal evolution during the early Earth. This evolution depends on thermal boundary conditions, thermal conductivity, etc. But the models of its behavior and relation to the crystals that start to form as the temperature drops below the liquidus are highly dependent on the thermal EOS of the melt.

The main differences between 3rd order EOS (BM3 and Vinet) and

the 4th order EOS (BM4) reside in the temperature variations of the EOS parameters. **Figure S1** and Fig. 3 show the temperature variation of the BM3 and BM4 parameters, respectively. BM3 fits in the 0–180 GPa pressure range show a non-linear decrease of the bulk modulus with temperature. Vinet also shows a change of slope in the dK/dT after 3500 K. Instead, BM4 fits yield excellent linear dK/dT fits of −6.8 MPa/K. Together with the quasi-linear thermal dilation, these can be used in the next step, within the Holland-Powell term, to fit thermal EOS. We can thus argue that, provided enough points are available for the EOS fit, BM4 should be the preferred choice of an EOS. Moreover, this linear relation could be potentially verified in experiments on the melt, at low temperatures.

With 128 reliable pressure – temperature – density points distributed over a wide temperature and pressure range (**Table S1**), we can reliably use a BM4 EOS (Eq. (1)) and the Holland-Powell expression for the thermal expansion (Eq. (2)) to describe the behavior of the magma ocean. This combination of athermal and thermal EOS yields the smallest standard deviation errors on the different fitted parameters. We employed the EOSFit software (Angel et al., 2014) to perform the fitting. The values of the different parameters are listed in Table 3.

3.2. Melt compressibility and the interatomic bonds

We can use our simulations to obtain a quick but reliable overview of the Si-O bond lengths in our melts as a function of pressure and temperature. The presence of 48 Si atoms in the unit cell, each surrounded by several O atoms, ensures sufficient statistics that allow us to obtain good pair distribution functions even for relatively short simulations, some of only 4 ps.

A few selected computed Si-O pair distribution functions along the 4000 K isotherm are plotted in Fig. 4. The allure of the g(r) are smooth, with a clear exclusion zone, a maximum corresponding to the most likely Si-O bond distance, and a first minimum corresponding to the radius of the first coordination sphere. As our simulation boxes are large, they contain and thus can adequately describe not only the first coordination sphere, but also the second coordination sphere. This allows us to perform a thorough analysis of the structure of the melt.

The pressure evolution of the first coordination sphere has been investigated in multiple previous studies on various silicates (Bajgain et al., 2015; Davis et al., 2022; de Koker et al., 2008; Nomura et al., 2011; Sanloup et al., 2013; Solomatova and Caracas, 2019, 2021). The simulations presented here show a reduction of only a few percent of the average Si-O bond along a given isotherm in the 0 – 150 GPa pressure range. This is consistent, but slightly smaller, than our previous

Table 3
The parameters of the 4th (BM4) order Birch-Murnaghan equations of state (Eq. (1)) with Holland-Powell thermal expansion (Eq. (2)). The values are obtained from the fitting over all the values spanning the entire 0 - 180 GPa pressure range and 2000 – 5500 K temperature range. The reference temperature (ref) is set at 2000 K, and the density ρ_{ref} is fixed at 2.45 g/cm3, value extracted directly from the MD simulations. The fit yields weighted χ^2=1.64.

Parameter	Unit	Value	St. dev.
ρ_{ref}	g/cm^3	2.45	fixed
K_{ref}	GPa	24.864	1.597
K'		4.197	0.270
K''		−0.087	0.022
dK/dT	MPa/K	−4.62	0.051
α_0	K^{-1}	23.385	5.178
α_1	K$^{-1/2}$	66.432	20.627

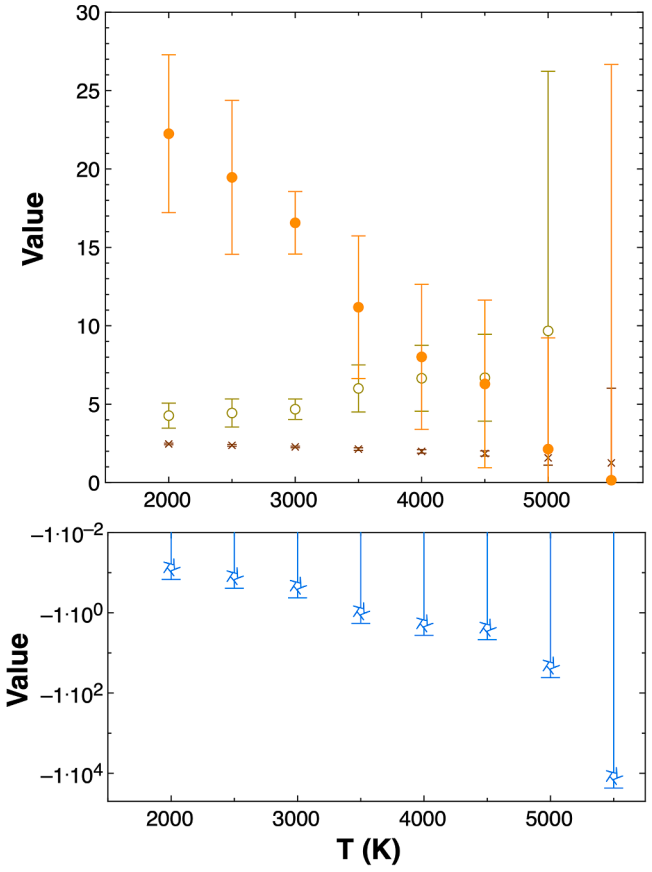

Fig. 3. Temperature variation of the different parameters of the 4th order Birch-Murnagham (BM) EOS. The athermal fits using the BM4 EOS show a linear temperature variation of the bulk modulus. The fits at 5500 K yield huge error bars, clearly showing the failure of standard BM fits for liquids close to the critical point. Crosses, filled circles, open circles, and diamonds correspond respectively to ρ_0 (g/cm3), K (GPa), K', and K''.

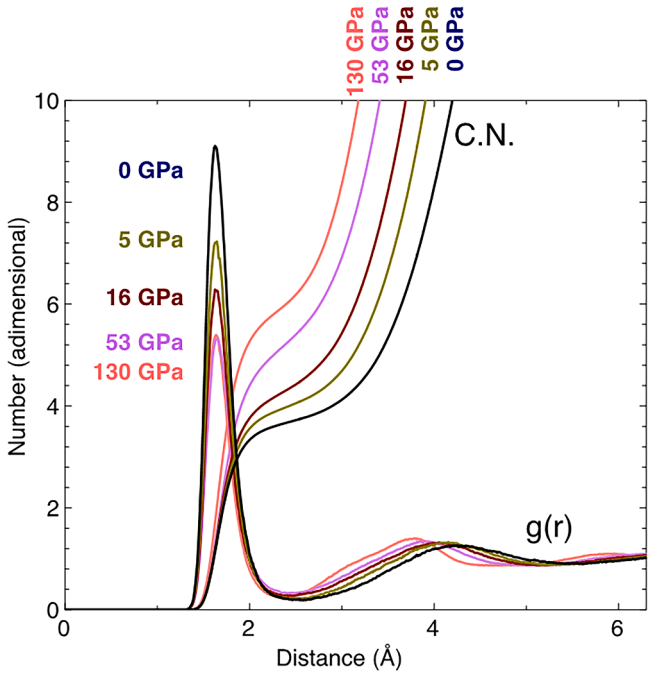

Fig. 4. Selected Si-O pair distribution functions at 4000 K and several pressures. The plots show two maxima corresponding to the first and second coordination spheres and two minima corresponding to the largest extent of the two coordination spheres. The computed pair distribution functions (g(r)) provide a solid numerical interpretation of the compressibility. Our simulations are sufficiently large to correctly describe not only the first Si -O coordination sphere but also the second sphere.

observations on pyrolite (Solomatova and Caracas, 2019). Snapshots of the structure at 4000 K are shown in **Figure S2**. The analysis of the structure of the melt is shown in Fig. 5 along the 4000 K isotherm. The height of the first peak of the g(r) is also almost constant in the same pressure range (Fig. 5a). The radius of the first coordination sphere shows a decrease up to about 20–30 GPa, followed by an almost constant behavior at higher pressures (Fig. 5b). The coordination number increases rapidly from 4 to 5 at 30 GPa and then slowly from 5 to about 6 at 150 GPa (Fig. 5d).

But the most dramatic changes under pressure occur in the second coordination sphere. While the collapse of the second coordination sphere has long been proposed in the literature as being responsible for the main mechanism of the silicate melt compressibility (Wolf and McMillan, 1995), most of the previous simulations had too few atoms in the simulation box to accommodate enough space that would describe correctly and independently the second coordination sphere, due to its large size. Otherwise, if the simulation box is too small, the periodical boundary conditions prevent an independent description of the second coordination sphere, as the atoms would simply bond to their own periodically repeated image. Our simulations contain, even at the highest compression, more than twice the radius of the second coordination sphere of Si by O.

Compared to the first peak of the g(r), the height of the second peak of the Si-O g(r) shows a rapid decrease of more than 30 % in the first 30 GPa compression range; beyond 30 GPa the height is almost constant at least up to 150 GPa. The radius of the 2nd coordination sphere decreases by about 10 % in the same pressure range, while above, it shows only a weak reduction.

Finally, the compression of the melt is clearly reflected in the increase of the 2nd coordination number. This increases from about 24 at 0 GPa up to about 35 at 30 GPa and 40 at 150 GPa. It is this compaction of the second coordination sphere that is the main responsible for accommodating the compression of the silicate melt.

3.3. Magma ocean viscosity

The measurements on peridotite melt in the 2000–2500 K temperature range and 2.8 – 13 GPa pressure range put the viscosity in the 19 to 130 mPa range (Liebske et al., 2005). Later measurements along the liquidus show a drop of almost one order of magnitude, from 38 mPa.s at 7 GPa down to 17 mPa.s at 25 GPa (Xie et al., 2021), but the temperature increases during this pressure range. Other measurements on various peridotitic melts at high pressures show viscosities in the 30–50 mPa.s range at pressures up to 14 GPa (Cochain et al., 2017).

But the viscosity of silicate melts drops exponentially with increasing temperature, according to Aarhenius laws (Richet, 1984). Hence, it is enough to have just a few anchor points along or close to, for example, the magma ocean adiabat to obtain a reliable representation of the viscous behavior of the entire magma ocean before crystals start to form. In one remarkable study, Bajgain and colleagues (Bajgain et al., 2022) deciphered the viscosity variation of molten basalt at conditions spanning the entire mantle pressure and temperatures. They showed that beyond a simple exponential temperature dependence of the viscosity, changes in the structure of the basaltic melt induce a change in rheological behavior, which takes place around 10 GPa.

Here, we only determined the viscosity at a few points. Geodynamical studies can then rely on the trend presented by molten basalt to estimate the viscosity of the magma ocean as a whole. An example of the self-correlation of shear stresses is shown in **Figure S3**. We obtain that at 2.62 g/cm^3, at 4000 K and 5.2 GPa, the viscosity of molten pyrolite is 0.7 $\pm$ 0.05 mPa.s, and at 4.13 g/cm^3, at 4000 K and 53.4 GPa, the viscosity of pyrolite is 1.9 $\pm$ 0.1 mPa.s. Thus, at least at the computed pressures and temperatures, the viscosity of liquid pyrolite is about half an order of magnitude below that of basalt at the same thermodynamic conditions.

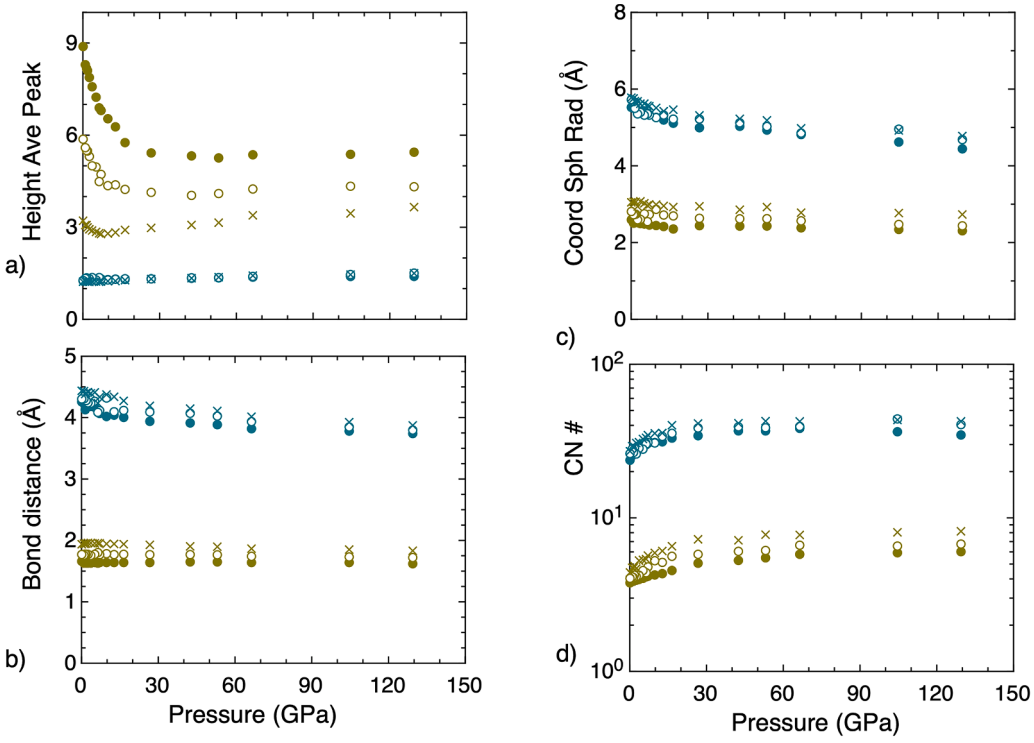

Fig. 5. The diagrams plotted here show, as a function of pressure: (a) the change in the height of the first peak of the g(r), corresponding to the most likely bond in the melt; (b) the radius of the 1st and 2nd coordination spheres; (c) the 1st and the (d) 2nd coordination numbers. The symbols correspond to Si-O (filled circles), Al-O (empty circles), and Mg-O (crosses). Olive is for the 1st coordination sphere, and teal is for the 2nd coordination sphere. The temperature of the simulations is 4000 K.

3.4. A revised critical point for the bulk silicate Earth

Finally, our newer, better simulations help us revisit the critical point of pyrolite (**Figure S4**). As the temperature approaches the critical temperature, previously estimated to be close to 6500 K for pyrolite (Caracas and Stewart, 2023), both BM3 and BM4 fail. At 6000 K, the density of pyrolite melt spans a 0.5–1.5 g/cm^3 density range over the 0 – 1 GPa pressure range. In this region, the pressure decreases almost monotonously with decreasing pressure. It reaches a flat region in the 0.61–0.88 g/cm^3. This behavior indicates that at this region, we are at or extremely close to the critical point. With clear dips and local minima in the pressure-density relation at 5500 K, and based on our previous experience with determining critical points, we suggest that the critical point of pyrolite should be decreased by at least 500 K with respect to the previous estimations. Based on these new larger simulations, we suggest it lies around 6000 K in the 0.6–0.88 g/cm^3 density range, at pressures of 1.1–1.2 kbars.

4. Implications and conclusions

We perform a large set of first-principles MD simulations studying melts with pyrolitic, bulk silicate Earth composition at thermodynamic conditions spanning the entire magma ocean stability field and beyond. Our calculations are spin-polarized, treat the electrons according to the Fermi-Dirac distribution, and contain simulation boxes with 306 atoms. The new simulations on the pyrolite melts have twice as many atoms as the previous ones and span a wider pressure and temperature range. With 128 points ranging between 2000 K and 0 GPa and 5500 K and 150 GPa, and with better treatment for the electronic temperature, they yield extremely reliable results, which can be used in further geodynamic modeling.

We report both athermal and thermal EOS. We obtain that the temperature variation of the bulk modulus in the BM4 EOS formulation is linear over the entire temperature range considered here, while in the 3rd order EOS formulation for both BM and Vinet, there is a change of slope around 3500 K. Then, we propose a unified thermal EOS. We find that the BM4 combined with the Holland-Powell description of the thermal dilatation gives the best fit to our computed data. We also revise the position of the critical point of the bulk silicate Earth by lowering its temperature by about 500 K. We suggest it lies around 6000 K, at pressures of 1.1–1.2 kbars.

These new estimations of lower critical temperature suggest that the protolunar disk that resulted from the Moon-forming giant impact could evolve even for longer times in the supercritical regime. With such longer times, the disk could be even better homogenized in terms of both chemical composition and isotope partitioning.

We complement the austere EOS fits with an analysis of the compressibility mechanism. We find a small contraction of the first coordination sphere accompanying the compression. With our large simulation cells, we can also reliably analyze the second coordination sphere of Si by O, avoiding the problems related to the periodic boundary conditions. This analysis shows that the compressibility of the pyrolite melts is accommodated by the collapse of the second coordination sphere. Along the 4000 K isotherm, the 2nd coordination number of Si by O almost doubles between 0 and 150 GPa.

Finally, we compute the shear viscosity of pyrolite liquid at two density points at 4000 K. We find that pyrolite is consistently less viscous than basalt by at least half an order of magnitude. Immediately following its condensation in the protolunar disk, we expect the turbulent regime to dominate the dynamics of the magma ocean. This is due both to the high temperatures and to the reduced viscosity. In this regime, the magma ocean would be extremely well mixed, where remnants of its previous history would have little or no chance of survival. Furthermore, it is only upon cooling below 4000 K that temperature-induced viscosity changes can play a role in the dynamics of the magma ocean.

With a low critical point and very low viscosity, we suggest that the protolunar disk and the magma ocean were ideal environments for mass, chemical, and isotopic mixing of all their constituents.

CRediT authorship contribution statement

Razvan Caracas: Writing – review & editing, Writing – original draft, Visualization, Validation, Supervision, Software, Resources, Project administration, Methodology, Investigation, Funding acquisition, Formal analysis, Data curation, Conceptualization.

Declaration of competing interest

The authors declare the following financial interests/personal relationships which may be considered as potential competing interests:

Razvan Caracas reports financial support was provided by Universite Paris Cite. Razvan Caracas reports financial support was provided by European Research Council. Razvan Caracas reports financial support was provided by Forskning.no. If there are other authors, they declare that they have no known competing financial interests or personal relationships that could have appeared to influence the work reported in this paper

Data availability

Data will be made available on request.

Acknowledgments

This research was made possible by support from the European Research Council under EU Horizon 2020 research and innovation program (ERC IMPACT grant agreement 681818), the project VADIS, financed by the LABEX UnivEarths of the UPC, the project HIDDEN (no. 223272) of the Research Council of Norway and through the Centres of Excellence funding scheme, project number 332523 (PHAB). I acknowledge access to supercomputing facilities via eDARI, grant no. stl2816 and the Sigma2/Uninet2, grant no. NN9697K.

Supplementary materials

Supplementary material associated with this article can be found, in the online version, at doi:10.1016/j.epsl.2024.118724.

References

Ahrens, T., 1995. Shock wave data for minerals. NASA-CR-199490.
Aksay, I.A., Pask, J.A., Davis, R.F., 1979. Densities of SiO2-AI2O3 Melts. J. American Chem. Soc. 62, 332–336.
Allen, M.P., Tildesley, D.J., 1987. Computer Simulation of Liquids. Clarendon Press, Oxford.
Angel, R.J., Alvaro, M., Gonzalez-Platas, J., 2014. EosFit7c and a Fortran module (library) for equation of state calculations. Z. Kristallogr. Cryst. Mater. 229, 405–419.
Asimow, P.D., 2012. Shock compression of preheated silicate liquids: apparent universality of increasing Grüneisen parameter upon compression. AIP Conf. Proc. 1426, 887–890.
Bajgain, S., Ghosh, D.B., Karki, B.B., 2015. Structure and density of basaltic melts at mantle conditions from first-principles simulations. Nat. Commun. 6, 8578.
Bajgain, S.K., Ashley, A.W., Mookherjee, M., Ghosh, D.B., Karki, B.B., 2022. Insights into magma ocean dynamics from the transport properties of basaltic melt. Nat. Commun. 13, 7590.
Ballmer, M.D., Lourenço, D.L., Hirose, K., Caracas, R., Nomura, R., 2017. Reconciling magma-ocean crystallization models with the present-day structure of the Earth's mantle. Geochem., Geophys., Geosys. 18, 2785–2806.
Baziotis, I., Xydous, S., Papoutsa, A., Hu, J., Ma, C., Klemme, S., Berndt, J., Ferrière, L., Caracas, R., Asimow, P.D., 2022. Jadeite and related species in shocked meteorites: limitations on inference of shock conditions. American Mineralog. 107, 1868–1877.
Birch, F., 1947. Finite elastic strain of cubic crystals. Phys. Rev. 71, 809–824.
Braithwaite, J., Stixrude, L., 2019. Melting of CaSiO(3) perovskite at high pressure. Geophys. Res. Lett. 46, 2037–2044.

Caracas, R., Hirose, K., Nomura, R., Ballmer, M.D., 2019. Melt–crystal density crossover in a deep magma ocean. Earth Planet. Sci. Lett. 516, 202–211.
Caracas, R., Kobsch, A., Solomatova, N.V., Li, Z., Soubiran, F., Hernandez, J.A., 2021. Analyzing melts and fluids from Ab Initio molecular dynamics simulations with the UMD package. J. Vis. Exp., e61534
Caracas, R., Mohn, C., Li, Z., 2023. Predicting HP-HT Earth and planetary materials, in: Bindi, L., Cruciani, G. (Eds.), Celebrating the international year of mineralogy: progress and landmark discoveries of the last decades, pp. 131–151.
Caracas, R., Stewart, S.T., 2023. No magma ocean surface after giant impacts between rocky planets. Earth Planet. Sci. Lett. 608, 118014.
Cochain, B., Sanloup, C., Leroy, C., Kono, Y., 2017. Viscosity of mafic magmas at high pressures. Geophys Res Lett 44, 818–826.
Cohen, R.E., Gong, Z., 1994. Melting and melt structure of MgO at high-pressures. Phys. Rev. B 50, 12301–12311.
Cohen, R.E., Weitz, J.S., 1998. The melting curve and premelting of MgO Properties of Earth and planetary materials at high pressure and temperature. In: Manghnani, M. H., Yagi, T. (Eds.), Geophysical Monograph, 1, pp. 185–196.
Davis, A.H., Solomatova, N.V., Campbell, A.J., Caracas, R., 2022. The speciation and coordination of a deep Earth carbonate-silicate-metal melt. J. Geophys. Res. Solid. Earth. 127, e2021JB023314.
de Koker, N., Karki, B.B., Stixrude, L., 2013. Thermodynamics of the MgO–SiO2 liquid system in Earth's lowermost mantle from first principles. Earth Planet. Sci. Lett. 361, 58–63.
de Koker, N.P., Stixrude, L., Karki, B.B., 2008. Thermodynamics, structure, dynamics, and freezing of Mg2SiO4 liquid at high pressure. Geochim. Cosmochim. Acta 72, 1427–1441.
Dodds, K.H., Bryson, J.F.J., Neufeld, J.A., Harrison, R.J., 2021. The thermal evolution of planetesimals during accretion and differentiation: consequences for dynamo generation by thermally-driven convection. J. Geophys. Res. Planets 126, e2020JE006704.
Elkins-Tanton, L.T., 2012. Magma oceans in the inner solar system. Annu. Rev. Earth Planet Sci. 40, 113–139.
Frenkel, D., Smit, B., 2002. Understanding Molecular Simulations. Academic Press.
Gonzalez-Cataldo, F., Davis, S., Gutierrez, G., 2016. Melting curve of SiO2 at multimegabar pressures: implications for gas giants and super-Earths. Sci. Rep. 6, 26537.
Greenwood, R.C., Franchi, I.A., Jambon, A., Buchanan, P.C., 2005. Widespread magma oceans on asteroidal bodies in the early Solar System. Nature 435, 916–918.
Hartley, M., Maclennan, J., 2018. Magmatic densities control erupted volumes in Icelandic volcanic systems. Front. Earth. Sci. (Lausanne) 6, 1–9.
Hernandez, J.A., Mohn, C.E., Guren, M.G., Baron, M.A., Trønnes, R.G., 2022. Ab Initio atomistic simulations of Ca-perovskite melting. Geophys. Res. Lett. 49, e2021GL097262.
Holland, T.J.B., Powell, R., 1998. An internally consistent thermodynamic data set for phases of petrological interest. J. Metamorph. Geol. 16, 309–343.
Hünenberger, P.H., 2005. Thermostat algorithms for molecular dynamics simulations. In: Advanced Computer Simulations, Advances in Polymer Science, pp. 105–149. Chapter 2.
Jephcoat, A.P., Besedin, S.P., 1996. Temperature measurement and melting determination in the laser-heated diamond-anvil cell. Philosoph. Transact. Royal Soc.-Math. Phys. Eng. Sci. 354, 1333–1360.
Kaminski, E., Limare, A., Kenda, B., Chaussidon, M., 2020. Early accretion of planetesimals unraveled by the thermal evolution of the parent bodies of magmatic iron meteorites. Earth Planet. Sci. Lett. 548, 116469.
Karki, B.B., 2010. First-principles molecular dynamics simulations of silicate melts: structural and dynamical properties. Rev. Mineral. Geochem. 71, 355–389.
Karki, B.B., Zhang, J., Stixrude, L., 2013. First principles viscosity and derived models for MgO-SiO2 melt system at high temperature. Geophys Res. Lett. 40, 94–99.
Kite, E., Kreidberg, L., Schaefer, L., Caracas, R., Hirschmann, M., 2021. Earth cousins" are new targets for planetary materials research. Eos. (Washington. DC)Eos. (Washington. DC) 102.
Kresse, G., Hafner, J., 1993. Ab initio molecular dynamics for liquid metals. Phys. Rev. B 47, 558–561.
Kresse, G., Joubert, D., 1999. From ultrasoft pseudopotentials to the projector augmented-wave method. Phys. Rev. B 59, 1758–1775.
Lange, R.A., Carmichael, I.S.E., 1987. Densities of Na20-K20-Ca0-Mg0-Fe0-Fe203-A1203-Ti02-Si02 liquids: new measurements and derived partial molar properties Geochirmica and Cosmochimica Acta 51, 293I–2946.
Liebske, C., Schmickler, B., Terasaki, H., Poe, B., Suzuki, A., Funakoshi, K., Ando, R., Rubie, D., 2005. Viscosity of peridotite liquid up to 13 GPa: implications for magma ocean viscosities. Earth Planet. Sci. Lett. 240, 589–604.
Liu, H., Wang, L., Xiao, X., De Carlo, F., Feng, J., Mao, H.K., Hemley, R.J., 2008. Anomalous high-pressure behavior of amorphous selenium from synchrotron x-ray diffraction and microtomography. Proc. Natl. Acad. Sci. u S. a 105, 13229–13234.
Mazevet, S., Tsuchiya, T., Taniuchi, T., Benuzzi-Mounaix, A., Guyot, F., 2015. Melting and metallization of silica in the cores of gas giants, ice giants, and super Earths. Physical Review B 92, 014105.
McDonough, W.F., Sun, S.s., 1995. The composition of the Earth. Chem. Geol. 120, 223–253.
Miller, G.H., Stolper, E.M., Ahrens, T.J., 2012. The equation of state of a molten komatiite: 1 Shock wave compression to 36GPa. J. Geophys. Res. 96, 11831–11848.
Moore, J.G., 2001. Density of basalt core from Hilo drill hole, Hawaii. J. Volcanol. Geothermal Res. 112, 221–230.
Morard, G., Hernandez, J.A., Guarguaglini, M., Bolis, R., Benuzzi-Mounaix, A., Vinci, T., Fiquet, G., Baron, M.A., Shim, S.H., Ko, B., Gleason, A.E., Mao, W.L., Alonso-Mori, R., Lee, H.J., Nagler, B., Galtier, E., Sokaras, D., Glenzer, S.H., Andrault, D., Garbarino, G., Mezouar, M., Schuster, A.K., Ravasio, A., 2020. In situ X-ray diffraction of silicate liquids and glasses under dynamic and static compression to megabar pressures. Proc. Natl. Acad. Sci. USA 117, 11981–11986.
Murakami, M., Bass, J.D., 2011. Evidence of denser MgSiO3 glass above 133 gigapascal (GPa) and implications for remnants of ultradense silicate melt from a deep magma ocean. Proc. Natl. Acad. Sci. USA 108, 17286–17289.
Murnaghan, F.D., 1944. The Compressibility of Media under Extreme Pressures. Proc. Natl. Acad. Sci. USA 30, 244–247.
Neumann, W., Breuer, D., Spohn, T., 2012. Differentiation and core formation in accreting planetesimals. Astron. Astrophy. 543, A141.
Nomura, R., Ozawa, H., Tateno, S., Hirose, K., Hernlund, J., Muto, S., Ishii, H., Hiraoka, N., 2011. Spin crossover and iron-rich silicate melt in the Earth's deep mantle. Nature 473, 199–202.
Perdew, J.P., Burke, K., Ernzerhof, M., 1996. Generalized gradient approximation made simple. Phys. Rev. Lett. 77, 3865–3868.
Petitgirard, S., Malfait, W.J., Sinmyo, R., Kupenko, I., Hennet, L., Harries, D., Dane, T., Burghammer, M., Rubie, D.C., 2015. Fate of MgSiO3 melts at core-mantle boundary conditions. Proc. Natl. Acad. Sci. USA 112, 14186–14190.
Prescher, C., Prakapenka, V.B., Stefanski, J., Jahn, S., Skinner, L.B., Wang, Y., 2017. Beyond sixfold coordinated Si in SiO(2) glass at ultrahigh pressures. Proc. Natl. Acad. Sci. USA 114, 10041–10046.
Ramo, D.M., Stixrude, L., 2014. Spin crossover in Fe2SiO4 liquid at high pressure. Geophys. Res. Lett. 41, 4512–4518.
Richet, P., 1984. Viscosity and configurational entropy of silicate melts. Geochim. Cosmochim. Acta 48, 471–483.
Rigden, S.M., Ahrens, T.J., Stolper, E.M., 1988. Shock compression of molten silicate: results for a model basaltic composition. J. Geophys. Res. 93, 367–382.
Sakamaki, T., Ohtani, E., 2022. High Pressure Melts. Rev. Mineral. Geochem. 87, 557–574.
Sanloup, C., 2016. Density of magmas at depth. Chem. Geol. 429, 51–59.
Sanloup, C., Drewitt, J.W., Konopkova, Z., Dalladay-Simpson, P., Morton, D.M., Rai, N., van Westrenen, W., Morgenroth, W., 2013. Structural change in molten basalt at deep mantle conditions. NatureNature 503, 104–107.
Schaefer, L., Elkins-Tanton, L.T., 2018. Magma oceans as a critical stage in the tectonic development of rocky planets. Phil. Trans. R. Soc. 376, 20180109.
Shi, C.Y., Zhang, L., Yang, W., Liu, Y., Wang, J., Meng, Y., Andrews, J.C., Mao, W.L., 2013. Formation of an interconnected network of iron melt at Earth's lower mantle conditions. Nat. Geosci. 6, 971–975.
Solomatova, N.V., Caracas, R., 2019. Pressure-induced coordination changes in a pyrolitic silicate melt from ab initio molecular dynamics simulations. J. Geophys. Res. Solid. Earth. 124, 11232–11250.
Solomatova, N.V., Caracas, R., 2021. Buoyancy and structure of volatile-rich silicate melts. J. Geophys. Res. Solid. Earth. 126, e2020JB021045.
Stagno, V., Kono, Y., Stopponi, V., Masotta, M., Scarlato, P., Manning, C.E., 2020. The Viscosity of Carbonate-Silicate Transitional Melts at Earth's Upper Mantle Pressures and Temperatures, Determined by the In Situ Falling-Sphere Technique, Carbon in Earth's Interior. John Wiley & Sons, Inc, pp. 223–236.
Stixrude, L., de Koker, N., Sun, N., Mookherjee, M., Karki, B.B., 2009. Thermodynamics of silicate liquids in the deep Earth. Earth Planet. Sci. Lett. 278, 226–232.
Stixrude, L., Karki, B., 2005. Structure and freezing of MgSiO3 liquid in Earth's lower mantle. Science (1979) 310, 297–299.
Sturtz, C., Limare, A., Tait, S., Kaminski, 2022a. Birth and decline of magma oceans in planetesimals: 1. Experimental study of erosion and deposition of particles in an internally heated convecting fluid. J. Geophys.Res.-Planet. 127, e2021JE007000.
Sturtz, C., Limare, A., Tait, S., Kaminski, É., 2022b. Birth and decline of magma oceans in planetesimals: 2. structure and thermal history of early accreted small planetary bodies. Journal of Geophysical Res. 127 e2021JE007020.
Suzuki, A., Ohtani, E., 2003. Density of peridotite melts at high pressure. Phys Chem Miner 30, 449–456.
Suzuki, A., Ohtani, E., Funakoshi, K., Terasaki, H., Kubo, T., 2002. Viscosity of albite melt at high pressure and high temperature. Phys. Chem. Miner. 29, 159–165.
Suzuki, A., Ohtani, E., Kato, T., 1998. Density and thermal expansion of a peridotite melt at high pressure. Phys. Earth Planet. Interiors 107, 53–61.
Taniuchi, T., Tsuchiya, T., 2018. The melting points of MgO up to 4 TPa predicted based on ab initio thermodynamic integration molecular dynamics. J. Phys. Condens. Matter. 30, 114003.
Thomas, C.W., Asimow, P.D., 2013. Direct shock compression experiments on premolten forsterite and progress toward a consistent high-pressure equation of state for CaO-MgO-Al2 O3-SiO2-FeO liquids. J. Geophys. Res. 118, 5738–5752.
Thomas, C.W., Liu, Q., Agee, C.B., Asimow, P.D., Lange, R.A., 2012. Multi-technique equation of state for Fe2SiO4melt and the density of Fe-bearing silicate melts from 0 to 161GPa. J. Geophys. Res. 117, B10206.
Usui, Y., Tsuchiya, T., 2010. Ab initio two-phase molecular dynamics on the melting curve of SiO2. J. Earth Sci. 21, 801–810.
Wolf, G.H., McMillan, P.F., 1995. Pressure effects on silicate melt structure and properties. In: Stebbins, J.F., McMillan, P.F., Dingwell, D.B. (Eds.), Structure, Dynamics and Properties of Silicate Melts. Mineralogical Society of America, pp. 505–562.
Xie, L., Yoneda, A., Katsura, T., Andrault, D., Tange, Y., Higo, Y., 2021. Direct viscosity measurement of peridotite melt to lower-mantle conditions: a further support for a fractional magma-ocean solidification at the top of the lower mantle. Geophys. Res. Lett. 48, e2021GL094507.
Yu, T., Prescher, C., Ryu, Y.J., Shi, F., Greenberg, E., Prakapenka, V., Eng, P., Stubbs, J., Kono, Y., Shen, G., Watson, H., Rivers, M.L., Sutton, S.R., Wang, Y., 2019. A Paris-edinburgh cell for high-pressure and high-temperature structure studies on silicate liquids using monochromatic synchrotron radiation. Minerals 9, 715.